Polymer Testing 109 (2022) 107529

Contents lists available at ScienceDirect

Polymer Testing

journal homepage: www.elsevier.com/locate/polytest

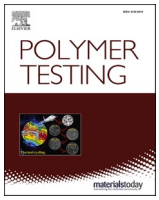

# Stiffness and damping behavior of 3D printed specimens

Francisco Medel [a,*], Javier Abad [a], Víctor Esteban [b]

[a] Department of Mechanical Engineering, Institute of Engineering Research of Aragón-I3A, Campus Río Ebro, School of Engineering and Architecture, Universidad de Zaragoza, Zaragoza, Spain
[b] Research Laboratory in Fluid Dynamics and Combustion Technologies (LIFTEC), CSIC-Universidad de Zaragoza, Zaragoza, Spain

ARTICLE INFO

*Keywords:*
Fused filament fabrication
3D printing
Laser Doppler vibrometry
Polylactic acid (PLA)
Mechanical properties
Elastic modulus
Damping ratio
Interfilament bonding

ABSTRACT

In this work, we analyzed a variety of metrics derived from Laser Doppler Vibrometry (LDV) characterization of 3D printed rectangular prisms. The metrics of interest were natural frequencies and amplitudes of first and second bending vibration modes, equivalent elastic moduli, damping ratios and areas of transmissibility functions. To explore the influence of printing process parameters on the dynamical behavior and, therefore, on the aforementioned metrics, 48 different combinations were considered, including build orientation, raster angle, nozzle temperature, print speed and layer height as relevant parameters. Thus, 96 polylactic acid (PLA) rectangular prisms were fabricated and LDV characterization was carried out. Based on the equivalent elastic modulus metrics, it was possible to corroborate the influence of printing process parameters on the mechanical performance, being raster angle, build orientation and nozzle temperature the most influential parameters. Likewise, the analysis of damping ratios served to assess the degree of interfilament bonding of 3D printed rectangular prisms. Thus, rectangular prims that exhibited high damping ratios also showed evident lack of adhesion between deposited filaments. Low damping ratios and, therefore, superior interfilament bonding was connected with on edge build orientation, high nozzle temperature (220 °C) and low print speed (60 mm/s) for specimens fabricated using 0° as raster angle. The analyses of areas of transmissibility functions and amplitudes of vibration modes also confirmed a better transmission of excitation (i.e., larger areas and higher amplitudes) for optimally fabricated parts, that is, specimens featuring relatively high equivalent elastic moduli and low damping ratios. Moreover, the application of Classical Laminate Theory to establish the relationships between elastic modulus and damping ratio with raster angle confirmed low temperature (200 °C) and high print speed (120 mm/s) resulted in low elastic modulus a high damping ratios and, therefore, poor interfilament bonding. The present findings confirm LDV is a powerful technique in the characterization of additively manufactured products, being able to discriminate different mechanical behaviors as well as the degree of interfilament bonding. Despite of their simplicity, the metrics derived from LDV characterization represent an attractive tool for both research and industrial applications.

## 1. Introduction

Additive manufacturing (AM) technologies have experienced a great development in the last decades [1–5]. In contrast to conventional subtractive manufacturing technologies, AM technologies produce parts by the addition of material, which in some cases is melted or cured, in a layer-by-layer fashion. The main advantages of AM technologies are that they make possible the fabrication of parts with complex geometries, require no specific tooling, reduce material waste and diminish fabrication times in the case of short series. Among AM technologies, Fused Filament Fabrication (FFF), also known as Fused Deposition Modelling (trademark registered by Stratasys), has attracted a great deal of interest at industrial, research and domestic levels [2,3,5]. FFF printers build parts by deposition of filaments of thermoplastic polymers, which are previously heated near the melting point and extruded through a nozzle [5]. Moreover, modern FFF printers often include two extruders, making possible the fabrication of parts using two different thermoplastic materials [6]. As for materials used for FFF, poly lactic acid (PLA) and acrylonitrile butadiene styrene (ABS) are the most popular materials [7–12], even though other thermoplastic materials and composites are now available, including high-performance polymers, such as poly-ether-ether-ketone (PEEK) and polyetherimide (PEI) [13–17]. The

* Corresponding author.
*E-mail address:* fjmedel@unizar.es (F. Medel).

https://doi.org/10.1016/j.polymertesting.2022.107529
Received 10 October 2021; Received in revised form 5 February 2022; Accepted 28 February 2022
Available online 3 March 2022

wide variety of thermoplastic filaments available for FFF and the versatility of this AM technology has raised interest in different research directions. The design and production of parts with overhanging features by using support material or not [18], fabrication of parts with two different materials (dual extrusion) [6], the static and dynamic mechanical performance of 3D printed parts [7–9,19–25], and bioprinting of human organ surrogates or implantable devices [26,27] are research fields, among others, that are rapidly developing.

As far as the mechanical performance of 3D printed specimens is concerned, it must be borne in mind that the mechanical properties of additively manufactured parts depend not only on the material (i.e., thermoplastic filament in FFF), but also on the printing process itself [12,19,28–30]. In the case of FFF, numerous printing variables can be custom adjusted to achieve the desired 3D printed part. Typically, build orientation, bead width, layer thickness, raster angle, air gap, print speed, bed temperature, infill density and infill pattern are the most relevant process parameters in FFF. Nevertheless, other process parameters may also have an impact on the integrity, mechanical performance and overall quality of 3D printed products. Thus, every individual set of printing variables is associated to a distinct mechanical behavior [19,31]. Despite the inherent complexity of the anisotropic mechanical behavior of additively manufactured parts, the scientific community has generated relevant knowledge about the mechanical properties of 3D printed products [12,28,32–35]. There is general agreement about the role of build orientation and raster angle, being the fabrication of parts using layers or filaments perpendicular to the load direction the most unfavorable from a mechanical point of view [19,20,28,32,33,36,37]. Similarly, higher infill densities and negative or zero air gaps have been associated with superior mechanical properties [9,20,38–43]. With regard to nozzle temperature, print speed, bed temperature and layer thickness, no total agreement has been reached, as apparently contradictory results have been reported. Thus, Song and coworkers and Aliheidari et al. pointed out that higher nozzle temperatures favored interfilament bonding and porosity reduction in 3D printed parts [44,45], whereas Abbott and collaborators concluded that print speed played a more significant role than extruder temperature, regarding tensile strength and contact length of ABS specimens [12]. Moreover, Yin and colleagues found that building stage temperature influenced the interfacial bonding strength between TPU and ABS in dual extrusion, but this was not the case for print speed or nozzle temperature [6]. A recent study by Basgul and colleagues has confirmed the importance of layer cooling times during FFF, proving that larger nozzle diameters and one-part printing batches are optimal conditions to achieve superior mechanical properties in 3D printed PEEK lumbar cages [14]. In addition, those researchers reported evidence of synergistic effects of low print speeds and post-printing annealing in the mechanical properties of 3D printed parts [15]. Low print speeds are probably behind a local heating effect because of the proximity of the extruder head to the part [12], but the role of this printing parameter in FFF has not been completely established. In any case, the influence of individual 3D printing process parameters, as well as their interactions in specific combinations, may configure the interfacial contact and intermolecular diffusion between adjacent filaments, allowing (or preventing) neck-growth and interfilament bonding [46]. In this sense, Liaw and coworkers have recently studied the interlayer bonding strength of 3D printed PEEK specimens, concluding that high nozzle temperature, short wait-time (that is, the time spent between printing of consecutive layers in the same part) and small layer height were preferable for greater stress at break, while print speed played a minor role [31]. Very recently, Basgul and coworkers have applied a heat transfer model to evaluate the degree of healing of layers while printing PEEK cuboids with two different commercial FFF machines. Based on their model, they conclude that the degree of healing can be enhanced increasing nozzle, bed and chamber temperatures [27]. More research is needed to completely ascertain the effects of printing process parameters on interfilament bonding and, therefore, interlayer strength and overall quality of 3D printed products.

In the previous context, the evaluation of the mechanical performance of 3D printed parts is paramount. Typically, static mechanical tests (tension, compression or flexural) have served to characterize the mechanical behavior of 3D printed products [6,7,9,12,20,24,28,38,40,44,47,48]. In contrast, the characterization of the structural dynamic behavior of additively manufactured parts is relatively scarce [21,24,25,39,49]. Laser Doppler Vibrometry (LDV) is a non-contact technique that permits the characterization of the dynamic behavior of a wide range of specimens or parts, providing their vibration response, that is, natural frequencies, damping, as well as real and imaginary parts of the modal constant [50,51]. The principle behind LDV is the detection of Doppler frequency shifts when light is scattered by a moving surface, as the frequency shift is proportional to the surface velocity. This technique is clearly advantageous for measuring lightweight structures without having to attach an accelerometer that can locally stiffen or mass load the structure [52]. LDV has been widely used in engineering applications, such as structural health monitoring, rotating machinery and acoustics. Thus, LDV successfully detected damaged regions (i.e. crack location) in beams and plates [52,53], delamination in composite structures [54], and the vibration behavior of rotating elements in different applications [55]. In recent years, LDV has also demonstrated its usefulness in the biomedical field, helping to characterize the vibration response of artificial and biological bones [56] and tympanic membranes [57,58]. Although the interest for the characterization of the vibration behavior of additively manufactured constructs, such as auxetic gradient honeycombs [59], multimaterial axially graded beams [60], partially unfused parts with high damping [61], lattice structures [62] or sandwich plates with 3D auxetic cores [63], is clearly growing, the use of LDV for dynamic characterization of 3D printed parts remains to be fully exploited. In our previous work, we demonstrated that LDV successfully discriminated between the mechanical properties (equivalent elastic modulus) of rectangular prisms produced by FFF using different printing process parameters combinations [19].

In the present work, we extend the analysis of our LDV characterization dataset of 3D printed rectangular prisms to a variety of metrics. These metrics are natural frequencies and amplitudes of the first and second bending modes, the corresponding equivalent elastic moduli and damping ratios, as well as the area of transmissibility frequency-response functions. Our hypotheses were that these metrics would serve, on one hand, to discriminate the influences of different printing process parameters combinations on the mechanical behavior (equivalent elastic moduli) and, on the other hand, to assess interfilament bonding (mainly via damping ratios) and overall quality of the 3D printed specimens. For this purpose, a design of experiments (DOE) approach was adopted, taking into account build orientation, nozzle temperature, raster angle, layer thickness and print speed as relevant printing process parameters. Thus, 48 different process parameters combinations were considered and two PLA rectangular prisms were fabricated for each individual combination ($n = 96$). Afterwards, LDV characterization was carried out to evaluate the structural dynamic behavior of the 3D printed rectangular prisms based on the aforementioned metrics. Finally, the classical laminate theory (CLT) was applied to describe both the stiffness and damping behavior of 3D printed rectangular prisms. In the following sections, a description of the 3D printing fabrication conditions, details about the Laser Doppler Vibrometry characterization and information about statistical analysis of the experimental metrics are provided first. Then, the basis of Classical Laminate Theory (CLT) is introduced to develop theoretical models of stiffness and damping capacity versus raster angle for 3D printed specimens. Afterwards, the main results corresponding to 1st and 2nd bending mode frequencies, equivalent elastic moduli, damping ratios, as well as areas and amplitudes of transmissibility functions are presented and discussed, identifying the main effects of the different process parameters combinations. Then, typical stiffness and damping behavior models obtained upon CLT application are shown and they are

connected with specific process parameters combinations. Finally, a summary of the study is given in the conclusions section.

## 2. Materials and methods

### 2.1. 3D printing fabrication

Rectangular prisms (90 x 7 × 2 $mm^3$) were designed using Solid Works (Dassault Systèmes; Paris, France). Then, the slicing software Cura (Ultimaker BV; Utrecht; The Netherlands) allowed conversion of STL files into G-code files. Subsequently, rectangular prisms were produced by FFF using a commercial 3D printer Ultimaker 3 Extended (Ultimaker BV; Utrecht; The Netherlands). A nozzle of 0.4 mm and 2.85 mm PLA filament spools were employed. To explore the influence of different process parameters combinations on the vibrational behavior of rectangular prisms, build orientation, nozzle temperature, layer height, print speed and raster angle were included in this study as main printing parameters. Based on a design of experiments (DOE) approach, two or three levels were taken into account for each of the previous parameters (see Table 1). Thus, the present study included 48 different combinations of 3D printing parameters and two rectangular prisms were fabricated for each combination, giving a total of 96 specimens. Other printing parameters were not considered as variables and they were set to default values when needed. For instance, the height and the printing speed of the initial layer, bed temperature or travel speed, among others, were set to 0.2 mm, 40 mm/s, 70 °C and 250 mm/s, respectively. To minimize fabrication time, on flat rectangular prisms were produced in six-samples batches, whereas on edge specimens were fabricated in two-sample batches. Evidently, the slicing preview provided by Cura was different depending on build orientation and raster angle (Fig. 1). Upon fabrication, rectangular prisms were measured in three different points to register their average nominal dimensions and to assess the deviation from theoretical dimensions [19].

### 2.2. Experimental characterization of vibrational behavior

The characterization of the vibrational behavior of 3D printed rectangular prisms was performed based on a cantilever beam configuration. Thus, a rectangular prism was clamped to a 2075 E shaker (The Modal Shop; Cincinnati, Ohio), leaving 70 mm of free length as cantilever beam. Then, the fixed end of the rectangular prism was subjected to a random broadband excitation, which had a Power Spectral Density of 0.05 $((m/s^2)^2/Hz)$, covered a frequency range from 10 to 1000 Hz and had a Root Mean Square equals to 7.036 $ms^{-2}$. The control of the input vibration signal was possible using a T333B30 accelerometer (PCB; Depew, New York), so that stimulation of out-of-plane bending vibration modes was achieved. The vibration response at the free end was measured using a PDV10 single-point laser vibrometer (Polytec; Waldbronn, Germany; Fig. 2). The registration and digital processing of the signals was completed by means of a PULSE™ system (Brüel&Kjaer; Nærum, Denmark), which consists of a data acquisition frontend (Type 3560-C) and the PULSE software version 9.2. In addition, it provided the Transmissibility Frequency Response Function for each rectangular prism, upon Fast Fourier Transform analysis of the signals with 6400 lines of resolution, an analysis range from 0 to 800 Hz, and averaging a hundred temporal measurements with an overlap of 66.67%. Finally, amplification factor versus frequency plots were generated for every 3D printed rectangular prism (Fig. 3a). Amplification factor – frequency plots provided different metrics, namely maximum amplitude, frequency at maximum amplitude and damping ratio for each vibration mode, as well as the area under the curve. Damping ratios, which are an indicator of damping behavior, were calculated based on the half power bandwidth method [64]. Thus, damping ratios were defined according to the following formula:

$$\xi_i = \frac{\Delta f_i}{2f_i} = \frac{f_2 - f_1}{2f_i} \quad (1)$$

Where $f_i$ is the resonance frequency of the corresponding vibration mode and $\Delta f_i$ is the bandwidth, at which the vibration amplitude decreases up to 3 dB, that is, this amplitude is the maximum amplitude by a factor of $\frac{1}{\sqrt{2}}$ (Fig. 3b).

The natural frequencies and average nominal dimensions of 3D printed rectangular prisms allowed computation of equivalent elastic modulus values for each vibration mode. The differential equation of motion for a solid, continuous and uniform, cantilever beam subjected to free lateral vibration may be written as:

$$\frac{\partial^2 w_0}{\partial t^2} + \frac{k_s}{\rho_s}\frac{\partial^4 w_0}{\partial x^4} = 0 \quad (2)$$

where $\rho_s$ is the mass per unit area and $k_s$ is the stiffness per unit area, which is given by:

$$k_s = \frac{1}{D_{11}^{-1}} = \frac{h^3 E}{12} \quad (3)$$

where $D_{11}^{-1}$ is the corresponding flexural compliance coefficient, h is the beam thickness and E the flexural elastic modulus.

Thus, the solution to the previous equation of motion of an undamped cantilever beam subjected to free lateral vibration relates the natural frequency of a particular vibration mode with material parameters according to the following formula [65]:

$$f_i = \sqrt{\frac{E \cdot J}{\rho \cdot A}}\ \frac{1}{2\pi}\left(\frac{k_i}{l}\right)^2 \quad (4)$$

where $f_i$ is the natural frequency of the considered vibration mode, E denotes the elastic modulus of the material, $k_i$ are constants related to the vibration mode (1.875 and 4.694 for the first and second bending vibration modes, respectively) and ρ is the density of the material. A, l and J are the cross-sectional area of the beam, free length and the moment of inertia of the beam cross section, respectively.

Based on equation (4), an elastic modulus metric was computed for each 3D printed rectangular prism and for each vibration mode using the next formula:

$$E = \left(\frac{f_i \cdot 2\pi}{\left(\frac{k_i}{l}\right)^2}\right)^2 \cdot \frac{\rho \cdot A}{J} \quad (5)$$

Therefore, every 3D printed, partially solid, rectangular prism had two different metrics, one from each bending vibration mode, of its mechanical behavior from an elastic modulus perspective. These elastic modulus metrics did not represent a material property, but equivalent elastic moduli that include both the contributions of the deposited filaments and the interfilament bonding material, which have different elastic moduli.

**Table 1**
3D printing process parameters considered in the present study.

| 3D Printing parameters | | | | | | | | | | |
|---|---|---|---|---|---|---|---|---|---|---|
| Build Orientation | | Layer height (mm) | | Nozzle Temperature (°C) | | Print speed (mm/s) | | Raster angle (°) | | |
| On flat | On edge | 0.1 | 0.25 | 200 | 220 | 60 | 120 | 0 | 45 | 90 |

### 2.3. Statistical analysis

To confirm significant influences of 3D printing parameters on the

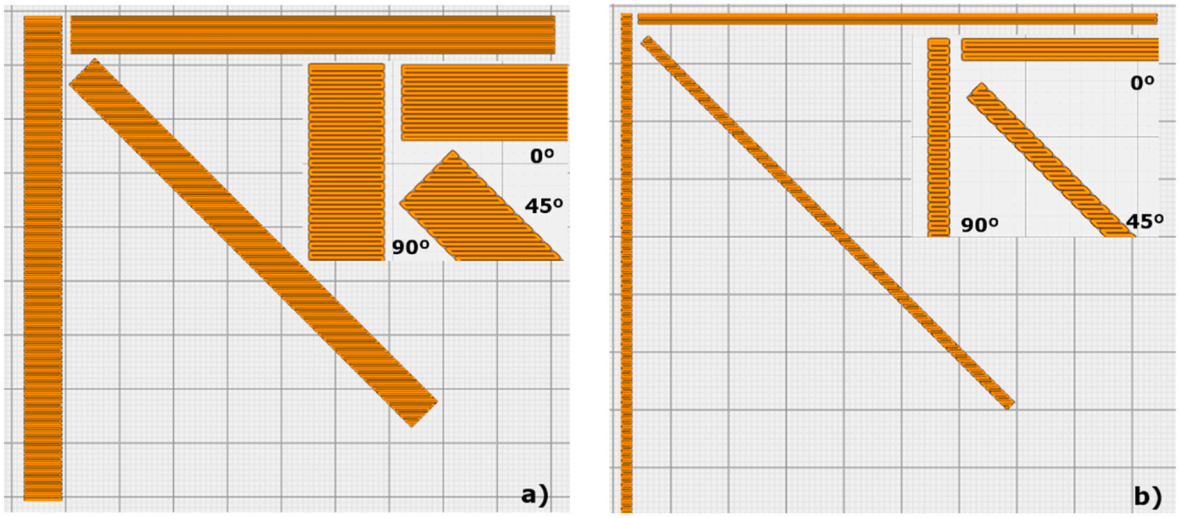


**Fig. 1.** Top view of the slicing preview provided by the software Cura (Ultimaker BV; Utrecht; The Netherlands) for rectangular prisms to be built on flat, a), and on edge, b). Filament deposition direction changes with raster angle.

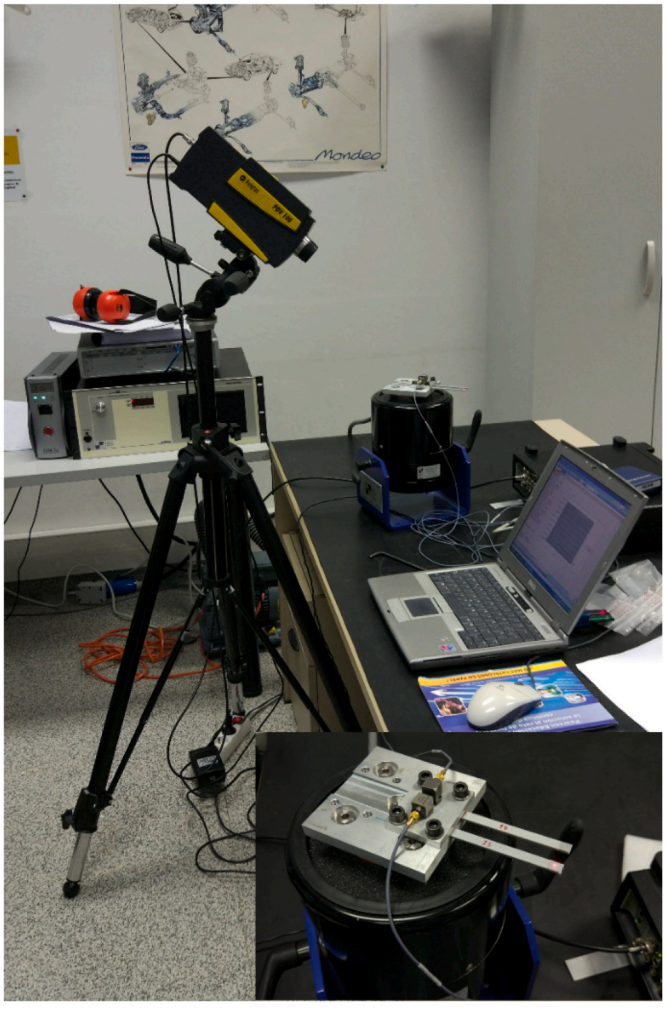


**Fig. 2.** Experimental set-up used for Laser Doppler Vibrational characterization of 3D printed specimens.

metrics extracted from LDV characterization of rectangular prisms, the present results were analyzed using JMP 13 software (SAS Institute; Cary, North Carolina). Thus, natural frequency, equivalent elastic modulus, damping ratio, area of transmissibility function and amplitude data were grouped by the process parameters of interest. The Shapiro-Wilk test served to confirm (or reject) the normality of data groups. Student's t-tests or Wilcoxon tests were employed to confirm significant differences between means of normally or non-normally, respectively, distributed data groups (level of significance $p < 0.05$). To help interpretation of the influence of 3D printing process parameters on the dynamic behavior of rectangular prisms, box plots of equivalent elastic modulus and damping ratio versus a specific 3D printing process parameter were prepared.

### 2.4. Stiffness and damping models derived from Classical Laminate Theory

The Classical Laminate Theory (CLT) describes the elastic behavior of laminated composites considering the constitutive equations of the lamina, the basic unit in the laminated composite [48,66,67]. In the case of 3D printing, a printed part may be identified as a laminated composite composed of several stacked layers (the laminae) and, therefore, its stiffness and damping behavior can be modelled according to CLT. In the case of an orthotropic lamina the strain-stress relationship written in material axes (1, longitudinal axis, 2, transversal axis and 3, axis normal to the lamina) is given by:

$$\begin{bmatrix} \varepsilon_1 \\ \varepsilon_2 \\ \varepsilon_6 \end{bmatrix} = \begin{bmatrix} S_{11} & S_{12} & 0 \\ S_{12} & S_{22} & 0 \\ 0 & 0 & S_{66} \end{bmatrix} \begin{bmatrix} \sigma_1 \\ \sigma_2 \\ \sigma_6 \end{bmatrix} \tag{6}$$

Where the components $S_{ij}$ are the compliance constants related to the engineering moduli, $E_L$, $E_T$, $G_{LT}$ and $\nu_{LT}$ by:

$$S_{11} = \frac{1}{E_L}\ ;\ S_{12} = -\frac{\nu_{LT}}{E_L}\ ;\ S_{22} = \frac{1}{E_T}\ ;\ S_{66} = \frac{1}{G_{LT}}\ . \tag{7}$$

Another approach is to consider the stress-strain relationship and the reduced stiffness tensor, which is related to the engineering moduli by:

$$\begin{bmatrix} \sigma_1 \\ \sigma_2 \\ \sigma_6 \end{bmatrix} = \begin{bmatrix} Q_{11} & Q_{12} & 0 \\ Q_{12} & Q_{22} & 0 \\ 0 & 0 & Q_{66} \end{bmatrix} \begin{bmatrix} \varepsilon_1 \\ \varepsilon_2 \\ \varepsilon_6 \end{bmatrix} = \begin{bmatrix} \frac{E_L}{1-\nu_{LT}\nu_{TL}} & \frac{\nu_{TL}E_L}{1-\nu_{LT}\nu_{TL}} & 0 \\ \frac{\nu_{TL}E_L}{1-\nu_{LT}\nu_{TL}} & \frac{E_T}{1-\nu_{LT}\nu_{TL}} & 0 \\ 0 & 0 & G_{LT} \end{bmatrix} \begin{bmatrix} \varepsilon_1 \\ \varepsilon_2 \\ \varepsilon_6 \end{bmatrix}; \tag{8}$$

With

$$\nu_{TL} = \nu_{LT}\frac{E_T}{E_L}; \tag{9}$$

So far, the axes refer to the lamina, but these axes may not be the same as the laminated composite axes. For that reason, it is useful to change from the lamina axes to the part axes, which allows introducing, $E_x$, Young's modulus measured in the x-direction of the laminated composite as:

$$S'_{11} = \frac{1}{E_x} = \frac{1}{E_L}\cdot\cos^4\theta + \frac{1}{E_T}\cdot\sin^4\theta + \left(\frac{1}{G_{LT}} - 2\frac{\nu_{LT}}{E_L}\right)\cos^2\theta\cdot\sin^2\theta; \tag{10}$$

With $\theta$ being the angle between the longitudinal axis of the lamina and the x-direction of the piece. In our experimental scheme, we fabricated rectangular prisms choosing 0°, 45° and 90° raster angles ($\theta$), so that the subsequent LDV characterization provided the longitudinal, shear and transversal moduli, respectively, for each printing set of a total of 16 printing groups. Based on equation (10) and the present experimental moduli, we calculated the analytical variation of $E_x$ with raster angle for the 16 printing groups included in this study. A value of 0.36 was used for PLA's longitudinal-transversal Poisson ratio to complete the aforementioned calculations.

As far as damping behavior is concerned, Adams and Bacon considered that the strain energy stored in a volume element, $\delta V$, of a laminated composited can be separated into three components associated to the stresses expressed in the lamina axes as [66,68]:

$$\delta U = \delta U_{11} + \delta U_{22} + \delta U_{66}; \tag{11a}$$

With

$$\delta U_{11} = \tfrac{1}{2}\sigma_1\varepsilon_1\delta V = \tfrac{1}{2}\sigma_1(S_{11}\sigma_1 + S_{12}\sigma_2)\delta V; \tag{11b}$$

$$\delta U_{22} = \tfrac{1}{2}\sigma_2\varepsilon_2\delta V = \tfrac{1}{2}\sigma_2(S_{12}\sigma_1 + S_{22}\sigma_2)\delta V; \tag{11c}$$

$$\delta U_{66} = \tfrac{1}{2}\sigma_6\varepsilon_6\delta V = \tfrac{1}{2}\sigma_6^2 S_{66}\delta V; \tag{11d}$$

Thus, the total energy stored in the laminated composite can be considered as the energy stored in the longitudinal direction, $\delta U_{11}$, the transverse direction, $\delta U_{22}$ , and in the in-plane shear, $\delta U_{66}$. Then, the strain energy dissipation in the longitudinal and transverse directions, as well as in the in-plane shear are written as:

$$\begin{aligned}\delta(\Delta U_{11}) &= \psi_{11}\delta U_{11};\\ \delta(\Delta U_{22}) &= \psi_{22}\delta U_{22};\\ \delta(\Delta U_{66}) &= \psi_{66}\delta U_{66};\end{aligned} \tag{12}$$

Where $\psi_{11}$ , $\psi_{22}$ and $\psi_{66}$ are the longitudinal, transverse and in-plane shear specific damping capacities, respectively. Then, the total energy dissipated in the element is the sum of the previous terms:

$$\delta(\Delta U) = \delta(\Delta U_{11}) + \delta(\Delta U_{22}) + \delta(\Delta U_{66}); \tag{13}$$

This expression can be extended to the whole laminate to derive the total energy dissipation:

$$\Delta U = \int_V \delta(\Delta U); \tag{14}$$

and the specific damping capacity of the laminate is then:

$$\psi = \frac{\Delta U}{U}\ ; \tag{15}$$

The damping capacity of the laminate considering a specific vibration mode is related to the loss factor, $\eta$, and the damping ratio, $\xi$, according to:

$$\psi = 2\pi\eta = 4\pi\xi; \tag{16}$$

As in our 3D printed rectangular prisms filaments were deposited selecting different raster angles, again, it was convenient to change from lamina axes to the part axes. This can be achieved considering the following expression:

$$\psi(\theta) = \psi_{11}a_{11}(\theta) + \psi_{22}a_{22}(\theta) + \psi_{66}a_{66}(\theta); \tag{17}$$

where functions $a_{ij}(\theta)$ vary depending on the analysis. In our case, we considered these functions as:

$$\begin{aligned}a_{11}(\theta) &= \frac{1}{Q_{11}^{-1}}\left(Q_{11}'Q_{11}^{-1} + Q_{12}'Q_{12}^{-1} + Q_{16}'Q_{16}^{-1}\right)\times\left(Q_{11}^{-1}\cos^2\theta + Q_{16}^{-1}\sin\theta\cos\theta\right)\cos^2\theta;\\ a_{22}(\theta) &= \frac{1}{Q_{11}^{-1}}\left(Q_{11}'Q_{11}^{-1} + Q_{12}'Q_{12}^{-1} + Q_{16}'Q_{16}^{-1}\right)\times\left(Q_{11}^{-1}\sin^2\theta - Q_{16}^{-1}\sin\theta\cos\theta\right)\sin^2\theta;\\ a_{66}(\theta) &= \frac{1}{Q_{11}^{-1}}\left(Q_{11}'Q_{11}^{-1} + Q_{12}'Q_{12}^{-1} + Q_{16}'Q_{16}^{-1}\right)\times\left[2Q_{11}^{-1}\sin\theta\cos\theta - Q_{16}^{-1}\left(\cos^2\theta - \sin^2\theta\right)\right]\times\sin\theta\cos\theta;\end{aligned} \tag{18}$$

where the elements $Q_{ij}'$ are the reduced stiffness constants expressed in the laminated composite axes. These terms can be obtained using the transformation matrices for the stress and strain tensors, which are $T_1$ and $T_2$, respectively:

$$[Q'] = [T_1]^{-1}\cdot[Q]\cdot[T_2] \tag{19}$$

$$[Q'] = \begin{bmatrix}\cos^2\theta & \sin^2\theta & -2\cos\theta\sin\theta\\ \sin^2\theta & \cos^2\theta & 2\cos\theta\sin\theta\\ \cos\theta\sin\theta & -\cos\theta\sin\theta & \cos^2\theta - \sin^2\theta\end{bmatrix}\cdot[Q]\cdot\begin{bmatrix}\cos^2\theta & \sin^2\theta & \cos\theta\sin\theta\\ \sin^2\theta & \cos^2\theta & -\cos\theta\sin\theta\\ -2\cos\theta\sin\theta & 2\cos\theta\sin\theta & \cos^2\theta - \sin^2\theta\end{bmatrix}$$

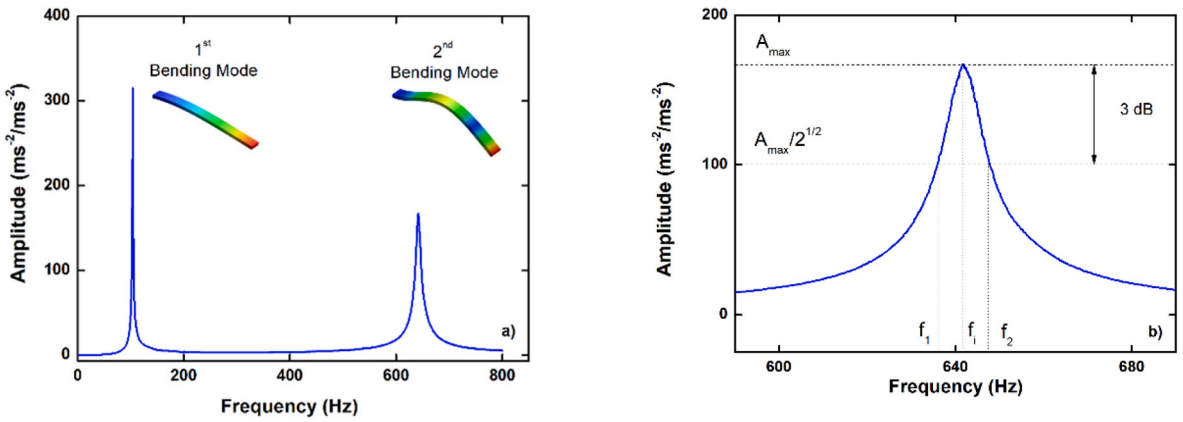


**Fig. 3.** Two bending vibration modes were studied using Laser Doppler Scanning Vibrometry. Damping ratios were calculated from amplitude vs frequency plots, a), based on the half power bandwidth method, b).

The previous theoretical framework was applied to describe the damping behavior of the present 3D printed specimens. Similarly to elastic modulus, the damping ratio measurements of additively manufactured prisms at 0, 45 and 90°, served to obtain an experimental measure of the longitudinal, $\psi_{11}$, transversal, $\psi_{22}$, and in-plane shear, $\psi_{66}$, specific damping capacities. These values, in turn, allowed determination of the analytical variation of the damping capacity of 3D printed prisms with raster angle, $\psi(\theta)$.

## 3. Results and discussion

### 3.1. Frequency and equivalent elastic modulus data

The frequency data provided by the present LDV characterization confirmed the influence of some process parameters on the dynamical behavior of 3D printed specimens. Thus, prisms fabricated on edge showed significantly higher frequencies in both, 1st and 2nd, bending modes than samples produced on flat (see Table 2). Nozzle temperature also demonstrated to have an impact, as specimens fabricated at 220 °C reached significantly higher frequencies than those produced at 200 °C (see Table 2). Finally, the selection of 0° as raster angle resulted in significantly higher frequencies with respect to samples fabricated at 45° (Table 2). Neither print speed nor layer height appeared to have a significant influence on the frequency behavior of 3D printed rectangular prisms.

The previous influence of build orientation, nozzle temperature and raster angle on both bending modes frequencies implied a similar effect on the corresponding equivalent elastic moduli (i.e., stiffness). In this case, raster angle was the most influential process parameter on this metric. Thus, 3D printed specimens built by depositing fused filaments at 0° reached the highest equivalent elastic moduli, as compared with specimens produced at 45° and 90° (see Table 2). Nozzle temperature also influenced the equivalent elastic modulus, as specimens fabricated at 220 °C had significantly higher moduli than those produced at 200 °C (Table 2). Build orientation had a significant influence on the 1st bending mode equivalent elastic modulus, as specimens built on edge were the stiffest. However, build orientation attained a marginally significant effect on the 2nd bending mode equivalent elastic modulus. The remaining process parameters, layer height and print speed had no statistically significant influences on the equivalent elastic moduli (Table 2). Boxplots of 2nd bending mode equivalent elastic modulus data grouped by the process parameters of interest are shown in Fig. 4a–c. Finally, it is worth noting that the 1st bending mode and 2nd bending mode equivalent elastic moduli were linearly correlated ($R^2 = 0.98$).

Frequency and equivalent elastic modulus results obtained from both bending modes corroborate the previously reported influences of 3D printing process parameters on the dynamical behavior [19]. Raster angle, nozzle temperature and build orientation were the most relevant parameters and, when properly selected, they were responsible for a shift to a higher frequencies, which implies higher equivalent elastic modulus (i.e. stiffness). The combination of on edge build orientation, 0° as raster angle, 200 °C nozzle temperature, layer height of 0.25 mm and 60 mm/s as print speed yielded the highest equivalent elastic modulus value for the 1st bending mode (3995 MPa). Likewise, on edge build orientation, 0° as raster angle, 220 °C nozzle temperature, layer height of 0.1 mm and 120 mm/s print speed reached the highest 2nd mode equivalent elastic modulus (3961 MPa).

The present results underline the importance of alignment of built layers and deposited filaments to the load direction, as previously reported [9,12,20,24,28,38,39,47,69,70]. Coherently, 3D printed specimens produced with filaments perpendicular to the stress axis demonstrated the poorest mechanical performance. Our analysis also confirmed the positive influence of higher nozzle temperatures on the mechanical behavior, in agreement with Aliheidari and coworkers and Liaw and collaborators [31,45]. Other studies have reported a minor influence of this process parameter [12], although this fact might stem from the temperature levels considered. Thus, the effect of nozzle temperature on the mechanical performance will be insignificant if all the temperature levels are beyond a threshold temperature. In our study, the extruder temperature levels were 200 and 220 °C and, since the detection of significant influences was possible, the threshold temperature appears to lie between those values.

We were not able to detect statistically significant effects of print speed and layer thickness on the frequency and elastic modulus behaviors. Regarding print speed, Basgul and coworkers reported no significant influences of print speeds (1500 and 2500 mm/min) on the ultimate strength of 3D printed PEEK cages, while other factors such as nozzle diameter and the number of parts produced per printing batch had a notable effect on mechanical strength [14]. According to those researchers, the effects of print speed might manifest when a threshold level is exceeded, with too high print speeds associated with decreased ultimate strength and increased porosity [71]. In contrast, Liaw and coworkers found that the strain at break of 3D printed PEEK specimens increased with print speed [31]. They pointed out that print speed mainly influences the intra-layer properties. Thus, higher print speeds

**Table 2**
Frequencies and equivalent elastic modulus data of 3D printed rectangular prisms grouped by the process parameters of interest. Average and standard deviation values are shown for every group. P values with asterisks (*) indicate statistically significant differences between the magnitudes above.

| | | 3D Printing parameters | | | | | | | | | | | |
|---|---|---|---|---|---|---|---|---|---|---|---|---|---|
| | | Build Orientation | | Layer height (mm) | | Nozzle Temperature (°C) | | Print speed (mm/s) | | Raster angle (°) | | | |
| | | On flat (n = 48) | On edge (n = 48) | 0.1 (n = 48) | 0.25 (n = 48) | 200 (n = 48) | 220 (n = 48) | 60 (n = 48) | 120 (n = 48) | 0 (n = 32) | 45 (n = 32) | 90 (n = 32) |
| **1st Bending Mode** | **Frequency (Hz)** | 79 ± 13 | 102 ± 18 | 92 ± 23 | 88 ± 16 | 85 ± 20 | 95 ± 18 | 90 ± 19 | 90 ± 21 | 96 ± 15 | 85 ± 23 | 90 ± 19 |
| | | P < 0.0001* | | P = 0.3832 | | P = 0.0069* | | P = 0.8922 | | P = 0.0228* (0-45) | P = 0.1489 (45-90) | P = 0.1729 (90-0) |
| | **Equivalent Elastic Modulus (MPa)** | 1866 ± 697 | 2369 ± 889 | 2158 ± 858 | 2078 ± 816 | 1905 ± 801 | 2331 ± 819 | 2150 ± 887 | 2085 ± 785 | 2856 ± 766 | 1695 ± 684 | 1802 ± 475 |
| | | P = 0.0058* | | P = 0.6417 | | P = 0.0078* | | P = 0.7722 | | P < 0.0001* (0-45) | P = 0.1997 (45-90) | P < 0.0001* (90-0) |
| **2nd Bending Mode** | **Frequency (Hz)** | 496 ± 85 | 616 ± 119 | 553 ± 138 | 554 ± 97 | 523 ± 127 | 586 ± 100 | 556 ± 108 | 550 ± 129 | 588 ± 110 | 515 ± 126 | 556 ± 111 |
| | | P < 0.0001* | | P = 0.9533 | | P = 0.0066* | | P = 0.8330 | | P = 0.0191* (0-45) | P = 0.1227 (45-90) | P = 0.1880 (90-0) |
| | **Equivalent Elastic Modulus (MPa)** | 1856 ± 692 | 2173 ± 864 | 1988 ± 839 | 2027 ± 751 | 1771 ± 717 | 2255 ± 796 | 2055 ± 802 | 1958 ± 786 | 2662 ± 838 | 1582 ± 567 | 1765 ± 449 |
| | | P = 0.0793 | | P = 0.6337 | | P = 0.0015* | | P = 0.4772 | | P < 0.0001* (0-45) | P = 0.2679 (45-90) | P < 0.0001* (90-0) |

might lead to a uniform layer with fewer voids. As for layer thickness, Liaw et al. have also found a significant effect of this parameter on elastic modulus [31]. It is worth mentioning that those authors included three layer height levels (0.1, 0.2 and 0.3 mm), so that they were capable of detecting a significant effect on the elastic modulus. In contrast, our study did not include the higher layer thickness (0.3 mm), for which smaller contact areas between deposited filaments and worse adhesion are expected. In general, good detection capabilities are anticipated for LDV in the case of print speed, layer thickness and wait-time provided enough levels are taken into account.

### 3.2. First and second bending modes damping ratios

The analysis of 1st bending mode damping ratio data confirmed raster angle was the most influential process parameter (see Table 3). Thus, specimens built selecting 90° as raster angle had significantly lower damping ratios than those fabricated at 45° and 0°. After raster angle, print speed had the most significant impact on damping behavior. Rectangular prisms fabricated at the lowest speed, 60 mm/s, exhibited significantly lower damping ratios than those produced at 120 mm/s (Table 3).

To find the underlying causes of the different damping behaviors, potential dependencies between damping ratio and stiffness were explored. Overall, 1st mode damping ratios did not correlate with the corresponding equivalent elastic moduli (see Fig. 5a). However, a decreasing trend of damping ratio with increasing equivalent elastic modulus was confirmed for specimens produced selecting 0° as raster angle (Fig. 5b). This trend suggested that 3D printed rectangular prisms that were fabricated better from an elastic modulus perspective also exhibited low damping ratios. This finding motivated the separate analysis of damping ratios for specimens built using 0° as raster angle. In the 0° subset, significantly lower damping ratios were attained selecting on edge orientation (Fig. 6a). Similarly, the highest nozzle temperature, 220 °C, resulted in the lowest damping ratios, whereas 3D printed specimens produced at 200 °C exhibited significantly higher damping ratios (Fig. 6b and Table 3). In addition, prisms built at the lowest print speed, 60 mm/s, had significantly lower damping ratios (Fig. 6c and Table 3). Finally, layer height demonstrated no significant effects on damping properties (Fig. 6d).

2nd bending mode damping ratios were, in average, generally higher than 1st mode damping ratios (see Table 3). However, statistical analyses confirmed no significant differences between them. Similar to 1st mode damping ratios, the use of raster angle equal to 0° yielded significantly higher 2nd mode damping ratios (Table 3). Build orientation also had a significant influence, as rectangular prisms built on edge had significantly lower damping ratios. The remaining process parameters appeared to have no significant influences on the damping behavior of this mode.

The previous damping ratio metrics were successful in discriminating the damping capacity of 3D printed specimens. This behavior is most probably connected with the degree of inter-filament bonding. In this sense, Rahman pointed out that damping in flax-fibre reinforced composites is attributed to the viscoelastic nature of matrix and/or reinforcement materials, the quality of the matrix-reinforcement interface, the presence of cracks, delamination and damaged fibers, friction due to slip in unbounded regions, the presence of pores and nonlinear effects at high stresses or strains [72]. In our study, the interface between filaments was judged the key factor in damping behavior, with lower damping ratios indicating superior interfilament bonding. Our damping ratios results suggest that enhanced bonding was achieved when shorter struts were selected to fill up the part. The worst-case scenario, printing at 0°, entails much longer struts, which makes more difficult to attain a homogeneous interface. Coherently, 3D printed specimens built at 0° showed the highest damping ratios, suggesting that interfilament bonding was not successfully achieved. Among specimens built at 0°, positive and significant influences of on edge build

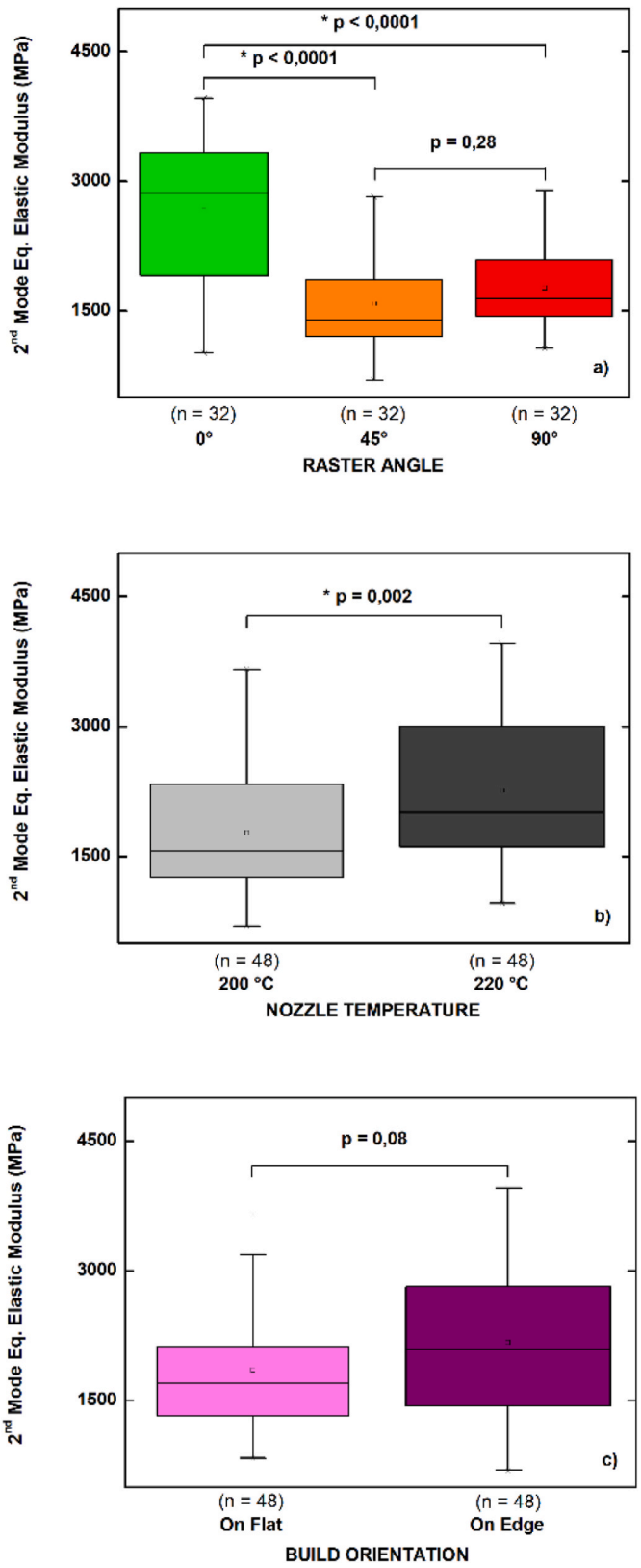


**Fig. 4.** Influence of 3D printing process parameters on the 2nd bending mode equivalent elastic modulus: raster angle, a), nozzle temperature b), and build orientation, c). Raster angle was the most influential parameter (significantly stiffer prisms were produced at 0°), followed by nozzle temperature, whereas build orientation had a marginally significant influence. Asterisks point out statistically significant differences between groups.

orientation, high nozzle temperature and low print speed were also confirmed, as they resulted in lower damping ratios. Moreover, the different quality of interfilament bonding achieved depending on the process parameters combination was visible to the naked eye. Thus, 3D printed rectangular prisms fabricated on flat, at 0°, 200 °C, 120 mm/s and 0.1 mm exhibited clear lack of adhesion and high damping ratios (Fig. 7a), whereas specimens built on edge, at 0°, 220 °C, 60 mm/s and 0.1 mm showed superior bonding and low damping ratios (Fig. 7b).

Achieving superior intralayer and interlayer bonding in 3D printed specimens is a complex goal, as various factors may have more of an impact. The importance of nozzle, bed and chamber temperatures has been recently highlighted [27], reporting a high degree of healing when high enough temperatures were used. Regarding the influence of print speed on interfilament bonding, Liaw and colleagues have suggested that higher print speeds might contribute to a better scenario for intralayer filament bonding, leading to a more uniform, less porous, layer [31]. However, too high print speeds have been associated with decreased mechanical properties and increased porosity [13,14], whereas the local heating effect due to the proximity between the extruder head and the part manifests at low print speeds [12]. Another factor affecting bonding is wait-time, which refers to the time spent between the deposition of a layer and the deposition of the next one in the same part. Typically, the higher number of specimens printed per run, the longer wait-times [31], so that deposited layers may cool down too much before the next layer is printed, affecting bonding quality. In our study, we found lower damping ratios at lower print speeds. This finding suggests that the highest speed included in our experimental design was too high, yielding a comparatively poorer interfilament bonding. In contrast, a local heating might take place at the lower print speed, resulting in superior bonding. Another important point to keep in mind is the different wait-times that on flat and on edge 3D printed rectangular prisms had in our study. Thus, wait-times between consecutive layers were longer for on flat specimens, since six prisms were built per run in that case, whereas two prisms were fabricated selecting on edge orientation. Nevertheless, LDV characterization was sensitive enough to discriminate specimens produced at each orientation from a damping behavior perspective. Thus, on edge specimens showed lower damping ratios, suggesting an enhanced interfilament bonding (see Figs. 6a and 7b). Finally, layer thickness did not affect damping performance in our study. Nevertheless, its influence cannot be completely ruled out, as layer height levels not included in this study ($\geq$0.3 mm) might decrease interfilament bonding.

Altogether, damping ratio results suggest that specimens fabricated with near optimum process parameters combination exhibited lower damping capacity (Table 4). In this regard, a more efficient transmission of excitation to rectangular is expected for optimally fabricated parts. Another point to bear in mind is that the 2nd bending mode is more demanding from a geometrical point of view. Thus, the 2nd mode demands higher compliance to rectangular prisms than the 1st mode. To explore the transmission of excitation, the area of transmissibility functions and the amplitude of vibration modes are analyzed in the following section.

### 3.3. Area of transmissibility functions and amplitude of vibration modes

3D printed specimens built on edge showed significantly larger areas than parts fabricated on flat (Table 5). Likewise, prisms built using 90° as raster angle had significantly larger areas than specimens produced at 45°. Despite showing a smaller average area, specimens printed at 0° were not significantly different from specimens built at 90° (Table 5). Finally, nozzle temperature exhibited a significant influence, as specimens printed at 220 °C showed significantly larger areas (Table 5). Layer height and print speed had no influence on this metric in the ranges considered in this study (Table 5).

Our analysis of the area of transmissibility functions data first explored correlations with elastic modulus data. In this sense,

**Table 3**
Damping ratios of 3D printed rectangular prisms grouped by the process parameters of interest. Average and standard deviation values are shown for every group. P values with asterisks (*) indicate statistically significant differences between the magnitudes above.

| | | 3D Printing parameters | | | | | | | | | | | |
|---|---|---|---|---|---|---|---|---|---|---|---|---|---|
| | | Build Orientation | | Layer height (mm) | | Nozzle Temperature (°C) | | Print speed (mm/s) | | Raster angle (°) | | | |
| | | On flat (n = 48) | On edge (n = 48) | 0.1 (n = 48) | 0.25 (n = 48) | 200 (n = 48) | 220 (n = 48) | 60 (n = 48) | 120 (n = 48) | 0 (n = 32) | 45 (n = 32) | 90 (n = 32) |
| 1st Bending Mode | Damping ratio (%) | 1.3 ± 0.7 | 1.1 ± 0.2 | 1.2 ± 0.6 | 1.1 ± 0.5 | 1.3 ± 0.7 | 1.1 ± 0.3 | 1.1 ± 0.6 | 1.2 ± 0.5 | 1.4 ± 0.8 | 1.2 ± 0.3 | 1.0 ± 0.2 |
| | | P = 0.1666 | | P = 0.1831 | | P = 0.5795 | | P = 0.0123* | | P = 0.5542 (0-45) | P = 0.0130* (45-90) | P = 0.0037* (90-0) |
| 2nd Bending Mode | Damping ratio (%) | 1.5 ± 1.3 | 1.2 ± 1.0 | 1.5 ± 1.3 | 1.3 ± 1.0 | 1.5 ± 1.5 | 1.2 ± 0.6 | 1.3 ± 1.2 | 1.5 ± 1.1 | 1.8 ± 1.7 | 1.3 ± 0.8 | 1.0 ± 0.1 |
| | | P = 0.0150* | | P = 0.1599 | | P = 0.5947 | | P = 0.1419 | | P = 0.0366* (0-45) | P = 0.1016 (45-90) | P = 0.0002* (90-0) |

representative transmissibility functions of low, intermediate and high equivalent elastic modulus specimens showed that the contributions to the area came, on one hand, from the amplitude, especially in the case of the 1st bending mode, and the width of vibration modes (Fig. 8).

However, a correlation between area and equivalent elastic modulus was not found. Nevertheless, the representation of these metrics suggested the area increased until an elastic modulus close to 2000 MPa was reached (Fig. 9). Moreover, the distinction of 3D printed specimens according to raster angle confirmed a linear increase of area with 2nd bending mode equivalent elastic modulus for parts produced at 0° ($R^2$ = 0.77; Fig. 9) and 45° ($R^2$ = 0.74).

Transmissibility functions have been widely applied to monitor the structural health of beam structures [73,74]. In these studies, the objective was to define a damage indicator from transmissibility functions that was able to detect the onset of damage in the structure. This damage indicator was obtained subtracting the transmissibility function of a damaged beam from that of the undamaged structure. Other researchers have used frequency response functions to evaluate the tool point dynamic repeatability for high-speed machining applications [75]. Thus, deviations from the baseline repeatability of frequency response functions allowed successful identification of changes in the tool setup. In our study, the analysis of the area of transmissibility functions helped to identify 3D printed specimens that were fabricated better from a structural point of view, even though a damage indicator or a baseline reference were not introduced. Thus, prisms exhibiting the largest areas also had relatively high equivalent elastic modulus, suggesting the transmission of excitation and, therefore, fabrication were better. As additive manufacturing technologies inherently produce porous parts, the study of transmissibility frequency response functions of 3D printed products may provide useful insight from a quality control perspective.

As for vibration amplitude behavior, build orientation was the most influential process parameter on the 1st bending mode amplitudes. Thus, 3D printed rectangular prisms built on edge having significantly higher amplitudes (Table 5). After build orientation, nozzle temperature also had an impact on the 1st mode amplitude, as samples produced at 220 °C displayed significantly higher amplitudes (Table 5). The remaining process parameters exhibited no significant influences.

Interestingly, the influences of process parameters on 2nd bending mode amplitudes were notably different. Thus, raster angle was the most influential process parameter, as rectangular prisms built depositing filaments at 90° showed significantly higher amplitudes (Table 5). This behavior might stem from the geometrical characteristics of the 2nd bending mode, for which relatively compliant specimens, those fabricated at 90°, are the ones that perform better. In addition, rectangular prisms built choosing a layer height of 0.25 mm exhibited significantly higher amplitudes (Table 5).

One of the main conclusions of the analysis of damping ratios was that low damping ratios were associated with superior interfilament bonding and relatively high elastic modulus, that is, with well-fabricated parts. Optimally fabricated parts are also expected to exhibit higher vibration amplitudes, based on the achievement of good interfilament bonding. For that reason, the relationship between damping ratios and amplitudes was explored. In the case of the 1st bending mode, no clear trends were detected (reciprocal fitting $R^2$ = 0.58; Fig. 10a). However, damping ratio and amplitude were inversely correlated for the 2nd bending mode (reciprocal fitting $R^2$ = 0.76; Fig. 10b). Moreover, the distinction of 3D printed specimens according to raster angle revealed that filament deposition at 90° implied simultaneously low damping ratios and high amplitudes for the 2nd mode (Fig. 10b). This finding suggests that most rectangular prisms produced at 90° were well-fabricated from both 2nd mode damping ratio and amplitude perspectives, although their equivalent elastic moduli were comparatively lower. As mentioned before, this behavior might stem from the more geometrically demanding characteristics of the 2nd bending mode. Thus, stiffer rectangular prisms (i.e. those fabricated at 0° and, therefore, with filaments aligned to the load direction) would not reach high

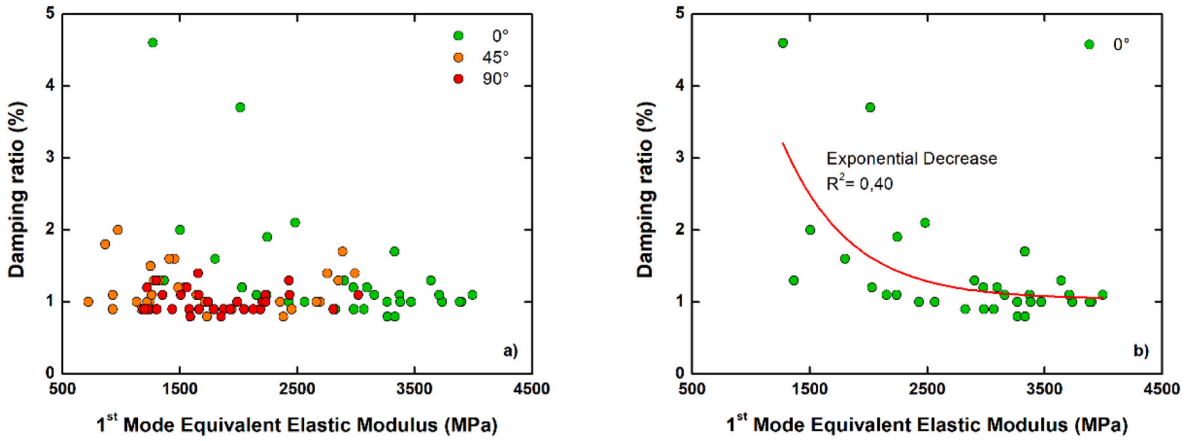


**Fig. 5.** Damping ratio versus equivalent elastic modulus dependency derived from the 1st bending mode. For this mode, damping ratios were not correlated with equivalent elastic modulus, with the only exception of specimens 3D printed at 0°, which showed a weak correlation.

amplitudes in the case of the 2nd bending mode, whereas more compliant 3D printed specimens (i.e. those fabricated at 90°) would perform better.

### *3.4. Stiffness and damping models based on the Classical Laminate Theory*

The equations derived from CLT allowed depicting the elastic modulus-raster angle dependency. Three distinct behaviors were observed upon application of CLT, regardless build orientation (Fig. 11). First, on flat process parameter combinations including high layer thickness and high nozzle temperature, as well as on edge printing sets featuring high temperature and high print speed, showed a decreasing, sigmoid-shaped, curve for both 1st and 2nd mode elastic moduli (Dark green lines in Fig. 11a and b). In these cases, small raster angles were associated with the highest elastic modulus (≥3000 MPa) and the minimum was reached close to 1000 MPa at 90°. Laminated composites, in which laminae consists of high modulus fibers and a low modulus

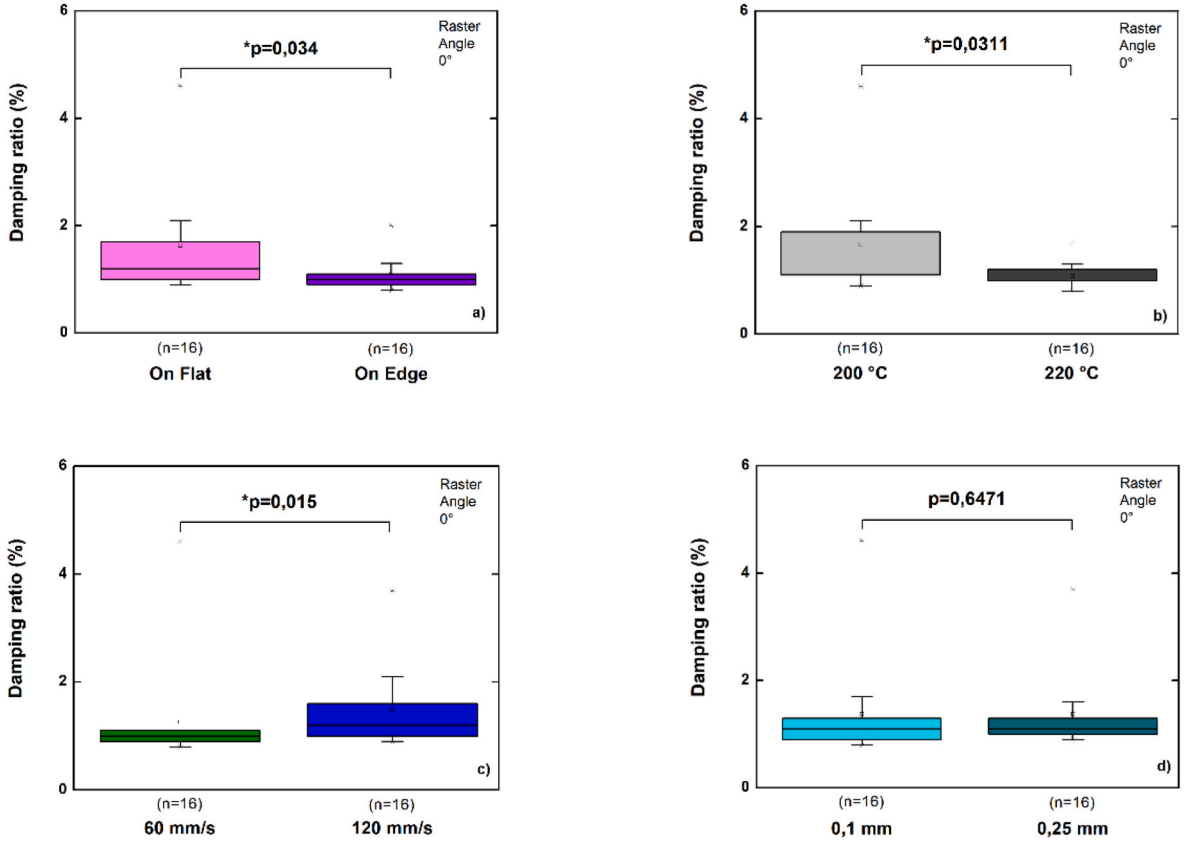


**Fig. 6.** Influence of 3D printing process parameters on the 1st mode damping behavior of specimens fabricated at 0°. Prisms printed using on edge build orientation, a), high nozzle temperature, 220 °C, b), and low print speed, 60 mm/s, c), exhibited significantly lower damping ratios. Contrariwise, layer height had no significant effects on damping capacity, d).

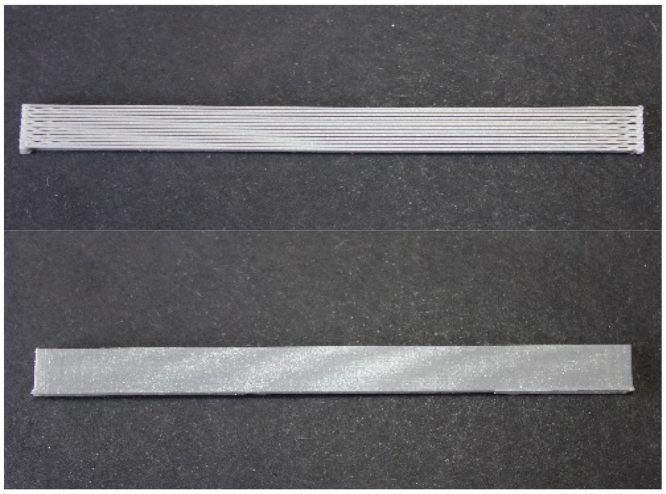

**Fig. 7.** 3D printed rectangular prisms built at 0° showed different degree of interfilament bonding depending on the remaining printing process parameters. Specimens fabricated on flat, at 0°, 200 °C, 120 mm/s and 0.1 mm (top) exhibited poor interfilament bonding and high damping ratio (2.1%), whereas the opposite was found for specimens fabricated on edge, at 0°, 220 °C, 60 mm/s and 0.1 mm (damping ratio 0.8%; bottom).

polymeric matrix, typically exhibit this behavior [66,67]. Likewise, this trend has been previously reported for specimens fabricated using FFF [25,48]. The second behavior exhibited the lowest elastic moduli, although some variation at 45° was present. This group was associated with low nozzle temperature and high print speed (Dotted lines in Fig. 11a and b). The third behavior was an intermediate or hybrid state, which started with high elastic modulus (>3000 MPa) at 0°, strongly decreased until a minimum (<2000 MPa) at 45° and ended with a light increase (2000 MPa) at 90°. A variety of process parameter combinations yielded this latter behavior, but most of them included the lowest print speed. Analyses of the 2nd bending mode elastic modulus CLT curves provided similar findings.

A variety of damping capacity behaviors was also noted upon application of CLT. Overall, the lowest damping ratios (≤1.5%) were associated with high nozzle temperature, regardless other process parameters (solid lines in Fig. 12 a-d). Contrariwise, the combination of low temperature and high print speed resulted in high damping ratios, especially at 0° (dotted lines in Fig. 12 a-d). This behavior was connected with evidence of poor interfilament bonding at the previously mentioned printing conditions (0°, 200 °C and 120 mm/s). Again, it is worth noting that selecting 0° as raster angle results in much longer deposited filaments and, therefore, in higher probability of bonding defects. Thus, higher raster angles were associated with lower damping ratios, even for the most adverse process parameter combinations. Regarding 2nd mode damping ratio CLT curves, they appeared to be more sensitive to printing conditions than the corresponding 1st damping ratio CLT curves. Thus, specimens fabricated using non-optimal process parameters combinations exhibited the highest damping ratios (from 2.7 up to 7.4%) at 0°. Overall, the damping capacity decreased or remained constant for the higher raster angles. The only exception was the use of on flat orientation, low layer thickness, high nozzle temperature and low print speed, which showed maximum damping capacity for a raster angle close to 30° (orange solid line in Fig. 12 c). Interestingly, Berthelot and Sefrani reported a very similar behavior for laminated composites [66]. As laminated composites combine a low modulus polymeric matrix and high modulus fibers, this fact suggests that deposited filaments using the aforementioned printing conditions reached good interfilament bonding, but with a low crystallinity interface region. Other printing process parameter combinations (see dark green solid lines in Fig. 12 a-d) probably resulted in good interfilament bonding and closer crystallinities for deposited filaments and interface regions.

Altogether, elastic modulus and damping CLT curves helped to identify suitable printing process parameters combinations. Thus, high elastic modulus and low damping ratio were indicators of optimal 3D printing fabrication. Nevertheless, we must keep in mind that 3D printed parts are not fully comparable to laminated composites. The interface region between filaments plays the role of matrix in 3D printed parts, but it is comparatively much scarcer. On the other hand, the elastic moduli of deposited filaments and interface regions are much closer than in laminated composites. In addition, CLT typically considers laminated composites composed of horizontally stacked layers, whereas 3D printed parts are built with layers stacked according to different configurations, depending on build orientation. In any case, LDV successfully characterized both the stiffness and damping behaviors of 3D printed specimens. Moreover, the analyses of the present experimental metrics, as well as the application of CLT, provided insight into the relationship between mechanical performance and 3D printing fabrication conditions.

In summary, all the metrics derived from LDV characterization demonstrated to be very useful in the inspection of mechanical performance and interfilament bonding of 3D printed specimens. The present findings confirm LDV is a very promising technique in the quality control of additively manufactured parts, with potential applicability at both research and industrial levels. Furthermore, this is, to the authors' knowledge, the first study to apply CLT to develop damping models for 3D printed specimens. Nevertheless, this study has a number of limitations. First, our experimental design did not cover all the 3D printing

**Table 4**
3D printing process parameters combinations exhibiting the lowest damping ratios. Manufacturing conditions yielding the highest equivalent elastic moduli are also shown.

| Build Orientation | Nozzle Temperature (°C) | Raster Angle (°) | Layer Height (mm) | Print Speed (mm/s) | Damping Ratios (%) | | Equivalent Elastic Modulus (MPa) | |
|---|---|---|---|---|---|---|---|---|
| | | | | | 1st Mode | 2nd Mode | 1st Mode | 2nd Mode |
| On flat | 220 | 90 | 0.25 | 60 | 0.8 | 0.9 | 1590 | 1751 |
| On flat | 220 | 45 | 0.25 | 120 | 0.8 | 0.9 | 2383 | 1959 |
| On edge | 220 | 0 | 0.1 | 60 | 0.8 | 0.9 | 3333 | 3340 |
| On edge | 220 | 0 | 0.1 | 120 | 1 | 1 | 3899 | 3961 |
| On edge | 200 | 0 | 0.25 | 60 | 1.1 | 2 | 3995 | 2819 |
| On edge | 200 | 90 | 0.25 | 60 | 0.8 | 0.9 | 1853 | 1069 |

**Table 5**
Area under the curve of transmissibility frequency response functions and amplitude values of the 1st and 2nd bending modes corresponding to 3D printed rectangular prisms. Average and standard deviation values are shown for every group. P values with asterisks (*) indicate statistically significant differences between the magnitudes above.

| | 3D Printing parameters | | | | | | | | | | | |
|---|---|---|---|---|---|---|---|---|---|---|---|---|
| | Build Orientation | | Layer height (mm) | | Nozzle Temperature (°C) | | Print speed (mm/s) | | Raster angle (°) | | | |
| | On flat (n = 48) | On edge (n = 48) | 0.1 (n = 48) | 0.25 (n = 48) | 200 (n = 48) | 220 (n = 48) | 60 (n = 48) | 120 (n = 48) | 0 (n = 32) | 45 (n = 32) | 90 (n = 32) |
| **AREA ($ms^{-2}/ms^{-2}$)*Hz** | 7264 ± 1468 | 8799 ± 2066 | 7985 ± 2144 | 8077 ± 1740 | 7455 ± 2166 | 8607 ± 1504 | 8200 ± 1583 | 7863 ± 2251 | 7785 ± 2217 | 7648 ± 1843 | 8661 ± 1622 |
| | P < 0.0001* | | P = 0.7250 | | P = 0.0032* | | P = 0.3982 | | P = 0.5063 (0-45) | P = 0.0365* (45-90) (Student's) | P = 0.2482 (90-0) |
| **1st Mode AMPLITUDE ($ms^{-2}/ms^{-2}$)** | 180 ± 83 | 319 ± 98 | 253 ± 130 | 246 ± 97 | 221 ± 123 | 278 ± 97 | 262 ± 114 | 237 ± 114 | 264 ± 121 | 218 ± 117 | 267 ± 101 |
| | P < 0.0001* | | P = 0.7333 | | P = 0.0121* | | P = 0.2775 | | P = 0.1065 (0-45) Student's | P = 0.0879 (45-90) (Student's) | P = 0.9245 (90-0) Student's |
| **2nd Mode AMPLITUDE ($ms^{-2}/ms^{-2}$)** | 162 ± 62 | 174 ± 54 | 156 ± 58 | 179 ± 57 | 163 ± 62 | 172 ± 54 | 177 ± 48 | 159 ± 66 | 132 ± 58 | 171 ± 55 | 200 ± 39 |
| | P = 0.1284 | | P = 0.0364* | | P = 0.6950 | | P = 0.3753 | | P = 0.0011* (0-45) | P = 0.0312* (45-90) | P < 0.0001* (90-0) |




**Fig. 8.** Representative transmissibility functions for 3D printed specimens featuring different equivalent elastic moduli (High and intermediate modulus curves have been vertically shifted for clarity). Stiffer specimens exhibited a shift to higher frequencies. Sharp vibration peaks were generally connected with larger areas, low damping behavior and optimal printing conditions.




**Fig. 9.** Influence of 2nd bending mode equivalent elastic modulus on the area of transmissibility functions of 3D printed specimens. Regardless raster angle, the area of transmissibility functions reached a plateau above an elastic modulus threshold close to 2000 MPa.

process parameters in FFF. Thus, air gap, bed temperature, extruder diameter, infill density and pattern, and number of shell perimeters, among others, were not considered and, when needed, they were set to default values. In this sense, previous studies have reported the significant influence of negative or zero air gaps, 100% solid infill density and larger nozzle diameters in achieving superior mechanical properties [14,20,24,38,41,42]. Second, our experimental plan included only two or three levels for the five printing process parameters considered, to make the study less time intensive. Thus, the potential influence of layer height in the LDV metrics could not be captured. As previously reported, layer thickness close to or higher than nozzle diameter may result in reduced contact areas between deposited filaments and, therefore, inferior mechanical properties [45]. Third, our approach to analyze the metrics derived from LDV characterization of 3D printed specimens has given priority to simplicity against the use of more refined methodologies, such as those based on the operating deflection shapes (ODS) and

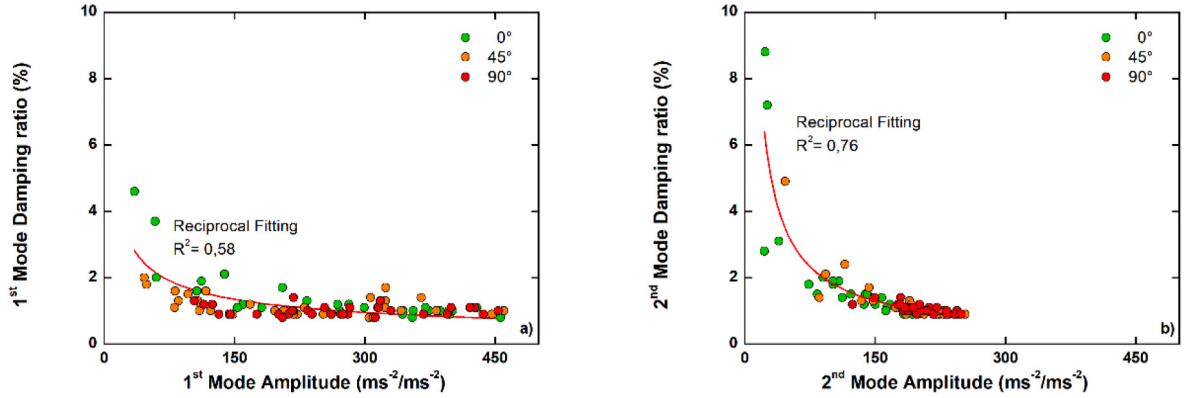


**Fig. 10.** Damping ratio and amplitude dependency of 3D printed specimens grouped by raster angle. The amplitude of the 1st vibration mode was not correlated with damping ratio. However, a strong amplitude-damping ratio correlation was found for the 2nd vibration mode, with specimens printed at 90° showing the lowest damping ratios and the highest amplitudes.

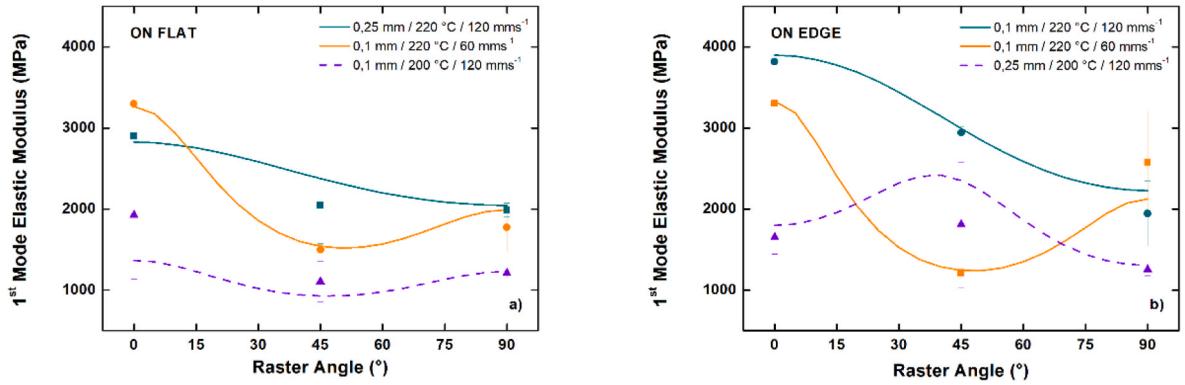


**Fig. 11.** 1st bending mode elastic modulus versus raster angle curves derived from Classical Laminate Theory (average experimental values are included as scatter points). Three different behaviors were noted: a decreasing, sigmoid-shaped, modulus (dark green lines), an overall low elastic modulus (violet dotted line) and an intermediate behavior (orange line). (For interpretation of the references to colour in this figure legend, the reader is referred to the Web version of this article.)

their corresponding curvatures [52,54]. In any case, the applicability of these LDV metrics in the additive manufacturing field appears very promising, for instance in the simulation and experimental assessment of novel 3D printed products featuring much more complex geometries, infill patterns or untested printing process parameters combinations for custom mechanical behavior.

## 4. Conclusions

In the present work, metrics extracted from LDV characterization served to assess the mechanical behavior, the degree of interfilament bonding and overall quality of 3D printed rectangular prisms. Thus, natural frequencies of 1st and 2nd bending modes allowed computation of the corresponding equivalent elastic moduli and identification of significant influences of process parameters (raster angle, nozzle temperature, etc.) on the mechanical behavior. Moreover, damping ratio data confirmed the association between high damping and poor interfilament bonding. In addition, it was possible to identify optimal values of 3D printing process parameters for low damping ratios and, therefore, enhanced interfilament bonding. Specifically, on edge build orientation, a nozzle temperature of 220 °C, a raster angle of 0°, a layer height of 0.1 mm and both print speed levels yielded simultaneously high elastic moduli (>3300 MPa) and low damping ratios (≤1%). On the other hand, data corresponding to areas of transmissibility functions and amplitudes of vibration modes revealed that optimally manufactured specimens exhibited larger areas and higher amplitudes. Despite of their simplicity, the metrics analyzed here have proved successful in the assessment of 3D printed specimens. Furthermore, the application of CLT to develop stiffness and damping models helped to identify different behaviors, depending on the 3D printing conditions. In particular, process parameters combinations including both low temperature (200 °C) and high print speed (120 mm/s) were associated with low equivalent elastic moduli and high damping ratios. In light of these results, LDV represents a powerful tool to characterize the mechanical properties and overall quality of additively manufactured products at both research and industrial levels. Further research on the use of LDV for characterization of 3D printed constructs designed for different applications (biomedical, automotive, etc.) and mechanical scenarios (torsion, compression, impact, fatigue, etc.) is warranted.

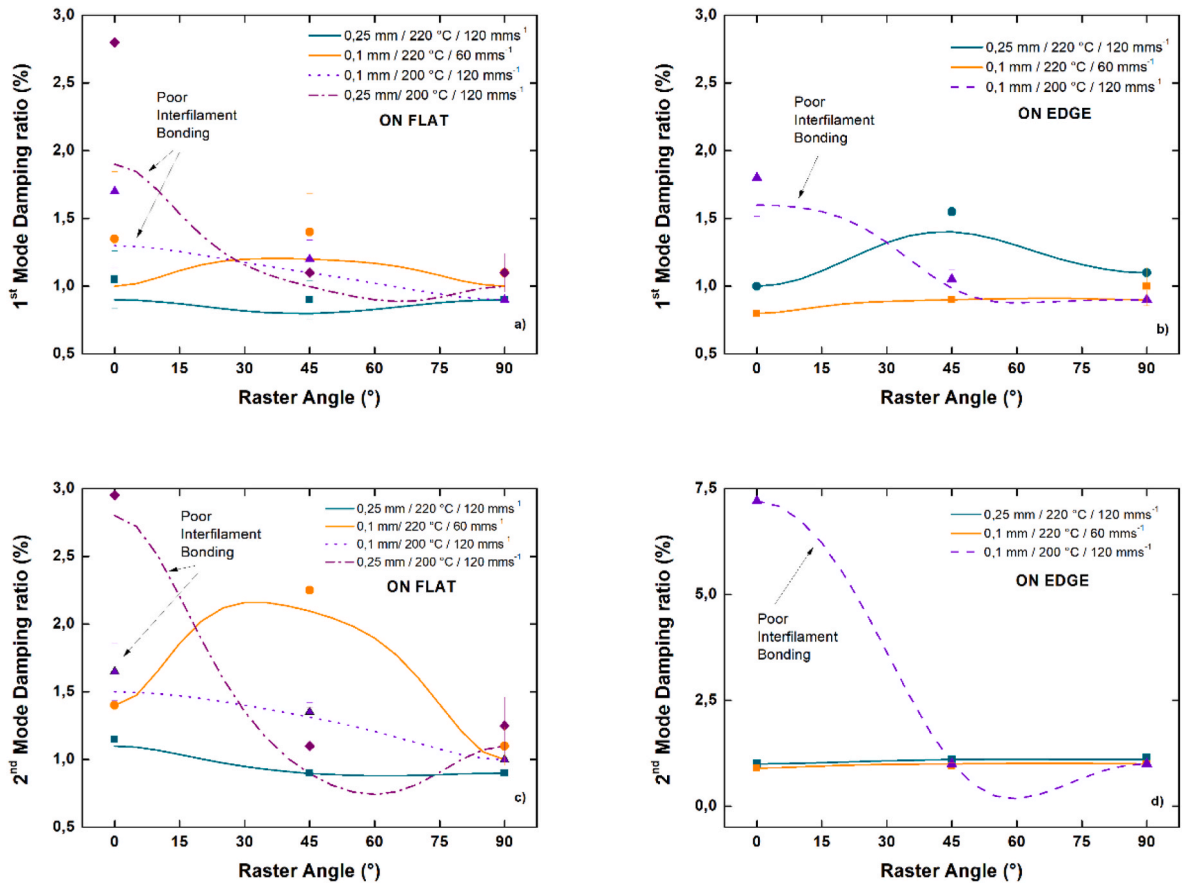


**Fig. 12.** 1st and 2nd modes damping ratios versus raster angle curves derived from CLT analysis (average experimental values are included as scatter points). High nozzle temperature typically resulted in low damping ratios (≤1.5%). Contrariwise, low nozzle temperature and high print speed resulted in high damping ratios (>1.5%) especially at 0°. This finding was connected with evidence of poor interfilament bonding.

## Data availability

The raw/processed data required to reproduce these findings cannot be shared at this time as the data also forms part of an ongoing study.

## CRediT authorship contribution statement

Francisco Medel: Conceptualization, Methodology, Formal analysis, Data curation, Writing - original draft, Writing – review & editing, Resources, Supervision. Javier Abad: Conceptualization, Methodology, Formal analysis, Data curation, Writing - review & editing, Resources. Víctor Esteban: Investigation, Formal analysis, Writing - review & editing.

## Declaration of competing interest

The authors declare that they have no known competing financial interests or personal relationships that could have appeared to influence the work reported in this paper.

## Acknowledgements

This study was supported by grants (Grupo de Biomateriales T48_20R and Grupo VEHIVIAL T19_20R) from Diputación General de Aragón (Spain).

## References

[1] W. Gao, Y.B. Zhang, D. Ramanujan, K. Ramani, Y. Chen, C.B. Williams, C.C. L. Wang, Y.C. Shin, S. Zhang, P.D. Zavattieri, The status, challenges, and future of additive manufacturing in engineering, Comput. Aided Des. 69 (2015) 65–89.
[2] B.N. Turner, R. Strong, S.A. Gold, A review of melt extrusion additive manufacturing processes: I. Process design and modeling, Rapid Prototyp. J. 20 (3) (2014) 192–204.
[3] B.N. Turner, S.A. Gold, A review of melt extrusion additive manufacturing processes: II. Materials, dimensional accuracy, and surface roughness, Rapid Prototyp. J. 21 (3) (2015) 250–261.
[4] J. Gardan, Additive Manufacturing Technologies State of the Art and Trends, Additive Manufacturing Handbook: Product Development for the Defense Industry, 2017, pp. 149–168.
[5] O.A. Mohamed, S.H. Masood, J.L. Bhowmik, Optimization of fused deposition modeling process parameters: a review of current research and future prospects, Adv. Manuf. 3 (1) (2015) 42–53.
[6] J. Yin, C.H. Lu, J.Z. Fu, Y. Huang, Y.X. Zheng, Interfacial bonding during multi-material fused deposition modeling (FDM) process due to inter-molecular diffusion, Mater. Des. 150 (2018) 104–112.
[7] B.M. Tymrak, M. Kreiger, J.M. Pearce, Mechanical properties of components fabricated with open-source 3-D printers under realistic environmental conditions, Mater. Des. 58 (2014) 242–246.
[8] A. Lanzotti, M. Grasso, G. Staiano, M. Martorelli, The impact of process parameters on mechanical properties of parts fabricated in PLA with an open-source 3-D printer, Rapid Prototyp. J. 21 (5) (2015) 604–617.
[9] S.H. Ahn, M. Montero, D. Odell, S. Roundy, P.K. Wright, Anisotropic material properties of fused deposition modeling ABS, Rapid Prototyp. J. 8 (4) (2002) 248–257.
[10] M. Dawoud, I. Taha, S.J. Ebeid, Mechanical behaviour of ABS: an experimental study using FDM and injection moulding techniques, J. Manuf. Process. 21 (2016) 39–45.
[11] B. Rankouhi, S. Javadpour, F. Delfanian, T. Letcher, Failure analysis and mechanical characterization of 3D printed ABS with respect to layer thickness and orientation, J. Fail. Anal. Prev. 16 (3) (2016) 467–481.
[12] A.C. Abbott, G.P. Tandon, R.L. Bradford, H. Koerner, J.W. Baur, Process-structure-property effects on ABS bond strength in fused filament fabrication, Add. Manuf. 19 (2018) 29–38.

[13] C. Basgul, T. Yu, D.W. MacDonald, R. Siskey, M. Marcolongo, S.M. Kurtz, Structure-property relationships for 3D printed PEEK intervertebral lumbar cages produced using fused filament fabrication, J. Mater. Res. 33 (14) (2018) 2040–2051.
[14] C. Basgul, D.W. MacDonald, R. Siskey, S.M. Kurtz, Thermal localization improves the interlayer adhesion and structural integrity of 3D printed PEEK lumbar spinal cages, Materialia (Oxf) 10 (2020).
[15] C. Basgul, T. Yu, D.W. MacDonald, R. Siskey, M. Marcolongo, S.M. Kurtz, Does annealing improve the interlayer adhesion and structural integrity of FFF 3D printed PEEK lumbar spinal cages? J. Mech. Behav. Biomed. Mater. 102 (2020), 103455.
[16] C. Basgul, H. Spece, N. Sharma, F.M. Thieringer, S.M. Kurtz, Structure, properties, and bioactivity of 3D printed PAEKs for implant applications: a systematic review, J. Biomed. Mater. Res. B Appl. Biomater. 109 (11) (2021) 1924–1941.
[17] M.A. Caminero, J.M. Chacon, E. Garcia-Plaza, P.J. Nunez, J.M. Reverte, J.P. Becar, Additive manufacturing of PLA-based composites using fused filament fabrication: effect of graphene nanoplatelet reinforcement on mechanical properties, dimensional accuracy and texture, Polymers 11 (5) (2019).
[18] M. Leary, L. Merli, F. Torti, M. Mazur, M. Brandt, Optimal topology for additive manufacture: a method for enabling additive manufacture of support-free optimal structures, Mater. Des. 63 (2014) 678–690.
[19] F. Medel, V. Esteban, J. Abad, On the use of laser-scanning vibrometry for mechanical performance evaluation of 3D printed specimens, Mater. Des. 205 (2021).
[20] A.K. Sood, R.K. Ohdar, S.S. Mahapatra, Parametric appraisal of mechanical property of fused deposition modelling processed parts, Mater. Des. 31 (1) (2010) 287–295.
[21] J. Lee, A. Huang, Fatigue analysis of FDM materials, Rapid Prototyp. J. 19 (4) (2013) 291–299.
[22] M. Domingo-Espin, S. Borros, N. Agullo, A.A. Garcia-Granada, G. Reyes, Influence of building parameters on the dynamic mechanical properties of polycarbonate fused deposition modeling parts, 3D Print. Addit. Manuf. 1 (2) (2014) 70–77.
[23] M. Domingo-Espin, J.M. Puigoriol-Forcada, A.A. Garcia-Granada, J. Lluma, S. Borros, G. Reyes, Mechanical property characterization and simulation of fused deposition modeling Polycarbonate parts, Mater. Des. 83 (2015) 670–677.
[24] S. Ziemian, M. Okwara, C.W. Ziemian, Tensile and fatigue behavior of layered acrylonitrile butadiene styrene, Rapid Prototyp. J. 21 (3) (2015) 270–278.
[25] C.W. Ziemian, R.D. Ziemian, K.V. Haile, Characterization of stiffness degradation caused by fatigue damage of additive manufactured parts, Mater. Des. 109 (2016) 209–218.
[26] B.K. Gu, D.J. Choi, S.J. Park, M.S. Kim, C.M. Kang, C.H. Kim, 3-dimensional bioprinting for tissue engineering applications, Biomater. Res. 20 (2016) 12.
[27] C. Basgul, F.M. Thieringer, S.M. Kurtz, Heat transfer-based non-isothermal healing model for the interfacial bonding strength of fused filament fabricated polyetheretherketone, Add. Manuf. 46 (2021).
[28] J.M. Chacon, M.A. Caminero, E. Garcia-Plaza, P.J. Nunez, Additive manufacturing of PLA structures using fused deposition modelling: effect of process parameters on mechanical properties and their optimal selection, Mater. Des. 124 (2017) 143–157.
[29] J.P. Oliveira, A.D. LaLonde, J. Ma, Processing parameters in laser powder bed fusion metal additive manufacturing, Mater. Des. 193 (2020) 12.
[30] P. Wang, B. Zou, H.C. Xiao, S.L. Ding, C.Z. Huang, Effects of printing parameters of fused deposition modeling on mechanical properties, surface quality, and microstructure of PEEK, J. Mater. Process. Technol. 271 (2019) 62–74.
[31] C.Y. Liaw, J.W. Tolbert, L.W. Chow, M. Guvendiren, Interlayer bonding strength of 3D printed PEEK specimens, Soft Matter 17 (18) (2021) 4775–4789.
[32] T.J. Gordelier, P.R. Thies, L. Turner, L. Johanning, Optimising the FDM additive manufacturing process to achieve maximum tensile strength: a state-of-the-art review, Rapid Prototyp. J. 25 (6) (2019) 953–971.
[33] B. Huang, S. Singamneni, Raster angle mechanics in fused deposition modelling, J. Compos. Mater. 49 (3) (2015) 363–383.
[34] J.R.C. Dizon, A.H. Espera, Q.Y. Chen, R.C. Advincula, O Mechanical characterization of 3D-printed polymers, Add. Manuf. 20 (2018) 44–67.
[35] D. Popescu, A. Zapciu, C. Amza, F. Baciu, R. Marinescu, FDM process parameters influence over the mechanical properties of polymer specimens: a review, Polym. Test. 69 (2018) 157–166.
[36] W.Z. Wu, P. Geng, G.W. Li, D. Zhao, H.B. Zhang, J. Zhao, Influence of layer thickness and raster angle on the mechanical properties of 3D-printed PEEK and a comparative mechanical study between PEEK and ABS, Materials 8 (9) (2015) 5834–5846.
[37] I. Durgun, R. Ertan, Experimental investigation of FDM process for improvement of mechanical properties and production cost, Rapid Prototyp. J. 20 (3) (2014) 228–235.
[38] A. Rodriguez-Panes, J. Claver, A.M. Camacho, The influence of manufacturing parameters on the mechanical behaviour of PLA and ABS pieces manufactured by FDM: a comparative analysis, Materials 11 (8) (2018).
[39] A.G. Salazar-Martin, M.A. Perez, A.A. Garcia-Granada, G. Reyes, J.M. Puigoriol-Forcada, A study of creep in polycarbonate fused deposition modelling parts, Mater. Des. 141 (2018) 414–425.
[40] D.W. Abueidda, M. Elhebeary, C.S. Shiang, S.Y. Pang, R.K. Abu Al-Rub, I.M. Jasiuk, Mechanical properties of 3D printed polymeric Gyroid cellular structures: experimental and finite element study, Mater. Des. 165 (2019).
[41] G. Gomez-Gras, R. Jerez-Mesa, J.A. Travieso-Rodriguez, J. Lluma-Fuentes, Fatigue performance of fused filament fabrication PLA specimens, Mater. Des. 140 (2018) 278–285.
[42] K.C. Ang, K.F. Leong, C.K. Chua, M. Chandrasekaran, Investigation of the mechanical properties and porosity relationships in fused deposition modelling-fabricated porous structures, Rapid Prototyp. J. 12 (2) (2006) 100–105.
[43] H. Rezayat, W. Zhou, A. Siriruk, D. Penumadu, S.S. Babu, Structure-mechanical property relationship in fused deposition modelling, Mater. Sci. Technol. 31 (8) (2015) 895–903.
[44] Y. Song, Y. Li, W. Song, K. Yee, K.Y. Lee, V.L. Tagarielli, Measurements of the mechanical response of unidirectional 3D-printed PLA, Mater. Des. 123 (2017) 154–164.
[45] N. Aliheidari, J. Christ, R. Tripuraneni, S. Nadimpalli, A. Ameli, Interlayer adhesion and fracture resistance of polymers printed through melt extrusion additive manufacturing process, Mater. Des. 156 (2018) 351–361.
[46] C. Bellehumeur, L. Li, Q. Sun, P. Gu, Modeling of bond formation between polymer filaments in the fused deposition modeling process, J. Manuf. Process. 6 (2) (2004) 170–178.
[47] S. Shaffer, K.J. Yang, J. Vargas, M.A. Di Prima, W. Voit, On reducing anisotropy in 3D printed polymers via ionizing radiation, Polymer 55 (23) (2014) 5969–5979.
[48] C. Casavola, A. Cazzato, V. Moramarco, C. Pappalettere, Orthotropic mechanical properties of fused deposition modelling parts described by classical laminate theory, Mater. Des. 90 (2016) 453–458.
[49] O.A. Mohamed, S.H. Masood, J.L. Bhowmik, Analytical modelling and optimization of the temperature-dependent dynamic mechanical properties of fused deposition fabricated parts made of PC-ABS, Materials 9 (11) (2016).
[50] S.J. Rothberg, M.S. Allen, P. Castellini, D. Di Maio, J.J.J. Dirckx, D.J. Ewins, B. J. Halkon, P. Muyshondt, N. Paone, T. Ryan, H. Steger, E.P. Tomasini, S. Vanlanduit, J.F. Vignola, An international review of laser Doppler vibrometry: making light work of vibration measurement, Opt Laser. Eng. 99 (2017) 11–22.
[51] D. Di Maio, P. Castellini, M. Martarelli, S. Rothberg, M.S. Allen, W.D. Zhu, D. J. Ewins, Continuous Scanning Laser Vibrometry: a raison d'& ecirc;tre and applications to vibration measurements, Mech. Syst. Signal Process. 156 (2021).
[52] D.M. Chen, Y.F. Xu, W.D. Zhu, Damage identification of beams using a continuously scanning laser Doppler vibrometer system, J. Vib. Acoust.Trans. Asme 138 (5) (2016).
[53] S.F. Zhao, S.J. Li, W. Guo, C.W. Zhang, B.W. Cong, Quantitative diagnosis method of beam defects based on laser Doppler non-contact random vibration measurement, Measurement 152 (2020).
[54] D.M. Chen, Y.F. Xu, W.D. Zhu, A comprehensive study on detection of hidden delamination damage in a composite plate using curvatures of operating deflection shapes, J. Nondestr. Eval. 38 (2) (2019).
[55] B.J. Halkon, S.J. Rothberg, Vibration measurements using continuous scanning laser vibrometry: advanced aspects in rotor applications, Mech. Syst. Signal Process. 20 (6) (2006) 1286–1299.
[56] C. Neupetsch, E. Hensel, M. Werner, S. Meißner, J. Troge, W.G. Drossel, C. Rotsch, Development and validation of bone models using structural dynamic measurement methods, Curr. Directions Biomed. Eng. 5 (1) (2019) 343–345.
[57] W.G. Engles, X.L. Wang, R.Z. Gan, Dynamic properties of human tympanic membrane after exposure to blast waves, Ann. Biomed. Eng. 45 (10) (2017) 2383–2394.
[58] J.A. Beyea, S.A. Rohani, H.M. Ladak, S.K. Agrawal, Laser Doppler Vibrometry measurements of human cadaveric tympanic membrane vibration, J. Otolaryngol. Head Neck Surg. 42 (2013).
[59] L. Boldrin, S. Hummel, F. Scarpa, D. Di Maio, C. Lira, M. Ruzzene, C.D.L. Remillat, T.C. Lim, R. Rajasekaran, S. Patsias, Dynamic behaviour of auxetic gradient composite hexagonal honeycombs, Compos. Struct. 149 (2016) 114–124.
[60] M. Heras Segura, K. Singh, F. Khan, A methodology for the design, fabrication and testing of axially graded polymeric structures with tailored vibration characteristics, Polym. Test. 94 (107054) (2021) 7.
[61] O. Scott-Emuakpor, J. Beck, B. Runyon, T. George, Determining unfused powder threshold for optimal inherent damping with additive manufacturing, Add. Manuf. 38 (2021).
[62] J.Q. Zhao, M. Zhang, Y. Zhu, X. Li, L.J. Wang, C.X. Hu, Concurrent optimization of additive manufacturing fabricated lattice structures for natural frequencies, Int. J. Mech. Sci. 163 (2019).
[63] C. Li, H.S. Shen, H. Wang, Z.F. Yu, Large amplitude vibration of sandwich plates with functionally graded auxetic 3D lattice core, Int. J. Mech. Sci. 174 (2020).
[64] G.A. Papagiannopoulos, G.D. Hatzigeorgiou, On the use of the half-power bandwidth method to estimate damping in building structures, Soil Dynam. Earthq. Eng. 31 (7) (2011) 1075–1079.
[65] S.S. Rao, Mechanical Vibrations, Pearson/Prentice Hall, 2004.
[66] J. Berthelot, Y. Sefrani, Damping analysis of unidirectional glass and Kevlar fibre composites, Compos. Sci. Technol. 64 (9) (2004) 1261–1278.

[67] J.N. Reddy, Mechanics of Laminated Composite Plates and Shells: Theory and Analysis, second ed. (second ed., CRC Press, Boca Raton, 2003.
[68] R. Adams, D. Bacon, Effect of fiber orientation and laminate geometry on dynamic properties of CFRP, J. Compos. Mater. 7 (OCT) (1973) 402–428.
[69] R. Gautam, S. Idapalapati, S. Feih, Printing and characterisation of Kagome lattice structures by fused deposition modelling, Mater. Des. 137 (2018) 266–275.
[70] C. Kousiatza, D. Tzetzis, D. Karalekas, In-situ characterization of 3D printed continuous fiber reinforced composites: a methodological study using fiber Bragg grating sensors, Compos. Sci. Technol. 174 (2019) 134–141.
[71] C. Basgul, T. Yu, D.W. MacDonald, R. Siskey, M. Marcolongo, S.M. Kurtz, Structure-property relationships for 3D-printed PEEK intervertebral lumbar cages produced using fused filament fabrication, J. Mater. Res. 33 (14) (2018) 2040–2051.
[72] M.Z. Rahman, Mechanical and damping performances of flax fibre composites – a review, Composites Part C: Open Access 4 (2021).
[73] L.L. Cheng, A. Cigada, An analytical perspective about structural damage identification based on transmissibility function, Struct. Health Monitor. Int. J. 19 (1) (2020) 142–155.
[74] W.J. Yan, D. Chronopoulos, K.V. Yuen, Y.C. Zhu, Structural anomaly detection based on probabilistic distance measures of transmissibility function and statistical threshold selection scheme, Mech. Syst. Signal Process. 162 (2022).
[75] K. Medicus, T. Schmitz, Evaluating the Tool Point Dynamic Repeatability for High-Speed Machining Applications, 16th Annual Meeting of the American Society for Precision Engineering, Arlington, VA, 2001.